Morphology Control of Indium Germanate Nanowires, Nanoribbons, and Hierarchical Nanostructures

Chaoyi Yan, Nandan Singh, and Pooi See Lee*

School of Materials Science and Engineering, Nanyang Technological University, Singapore 639798

ABSTRACT: We report morphology controlled syntheses of indium germanate nanostructures, including nanowires, ultralong nanoribbons, and hierarchical nanostructures. Proper selection and combination of the growth conditions such as catalyst, carrier gas, and source material was the key aspect to achieve morphology control. The as-synthesized nanostructures are single crystals with a monoclinic phase based on X-ray diffraction, scanning electron microscopy, and transmission electron microscopy characterizations. Vapor−liquid−solid, vapor−solid, and a combination of the two mechanisms were used to explain the growth of nanowires, nanoribbons, and hierarchical nanostructures, respectively.

1. Introduction

In recent years, there has been increasing interest in the synthesis of various one-dimensional (1D) nanostructures, such as nanotubes,[1] nanowires,[2] and nanoribbons.[3] Their unique geometries and novel properties make them ideal candidates for potential applications in nanoelectronics,[4] light emission,[5] energy conversion,[6] and chemical and biomedical sensors.[7] Central to realizing the versatile applications is the rational control of key nanomaterial parameters, including the size, structure, and morphology of the nanostructures. Extensive efforts have been devoted to synthesize 1D nanomaterials with controlled structures and morphologies.[8,9]

A clear understanding of the nanostructure formation mechanism is required in order to grow nanowires and nanoribbons with desired morphology or to design more complex structures such as branched[10] and hierarchical nanostructures.[11] The vapor−liquid−solid (VLS) mechanism has been most widely used for the growth of nanowires since it offers excellent control of the nanowire growth parameters.[12] Meanwhile, the vapor−solid (VS) mechanism based on a simple evaporation and condensation method is also usually used to explain the growth processes of 1D nanostructures.[3]

Germanates have attracted attention as important materials for catalysts, adsorption, ion exchange, humidity sensors, and high energy laser systems.[13−16] Several 1D indium germanate ($In_2Ge_2O_7$) nanostructures, such as microtubes,[17] nanoribbons,[18] and semi-nanotubes,[19] have been reported previously. However, controlled growth of $In_2Ge_2O_7$ nanostructures with variable morphologies has not been achieved until now, to the best of our knowledge. In this report, controlled growth of single crystalline $In_2Ge_2O_7$ nanostructures, including nanowires, ultralong nanoribbons, and hierarchical nanostructures, was successfully achieved by a thermal evaporation method. Proper selections and combinations of the growth conditions (catalyst, carrier gas, and source material) were the key aspects to achieve the morphology control. Detailed growth mechanisms for the various nanostructures are also discussed.

2. Experimental Section

The syntheses of indium germanate nanowires, nanoribbons, and hierarchical nanostructures were based on the vapor deposition process

in a conventional horizontal tube furnace. Morphology control of the nanostructures was realized by properly selecting the growth conditions as described below. In a typical experiment for $In_2Ge_2O_7$ nanowire synthesis, a small quartz tube containing mixed GeO_2, In_2O_3 and carbon powder (molar ratio 2:1:4) was loaded into the furnace. Si(100) substrates coated with 12 nm Au film were placed at the low-temperature end to collect the products. The central temperature of the furnace was increased to 1000 °C at a rate of 10 °C min⁻¹ and it was kept at that temperature for 60 min under a pure Ar flow of 200 sccm (standard cubic centimeter per minute). The furnace was then switched off and allowed to cool naturally to room temperature. For $In_2Ge_2O_7$ nanoribbon synthesis, keeping other experimental conditions unchanged, Ar gas mixed with 5% O_2 at a total flow rate of 200 sccm was used; clean Si substrates without Au coating were used for product collection. For three-dimensional (3D) hierarchical $In_2Ge_2O_7$ nanostructure synthesis, mixed Ge, In, and carbon powder (molar ratio 1:1:1) was used as source materials and other experimental conditions were kept the same as those for nanowire synthesis.

Morphology and structure of the products were characterized by X-ray diffraction (XRD, Rigaku) with Cu Kα radiation ($\lambda = 1.5418$ Å), field emission scanning electron microscopy (FESEM, JEOL 6340F), and transmission electron microscopy (TEM, JEOL 2010). For TEM analyses, the nanostructures were dispersed in ethanol by ultrasonication for 2 min, and then the solution was dropped on a copper grid coated with holey carbon film. Chemical compositions of the products were analyzed using energy dispersive spectroscopy (EDS) attached to the TEM system.

3. Results and Discussion

3.1. Indium Germanate Nanowire Growth. After the reaction, a layer of white product was found deposited on the substrate in the temperature range of 520−600 °C. The morphology of the as-synthesized products was first characterized using FESEM. Figure 1a is a typical top-view FESEM image of the nanowires. Dense nanowires tens of micrometers long grew on the Si substrate surface, and diameters of the nanowires are in the range of 20−80 nm. A representative FESEM image of nanowires growing at the edge of the substrates is shown in Figure 1b. XRD pattern of the nanowires is shown in Figure 1c. All the peaks belong to the monoclinic $In_2Ge_2O_7$ crystal phase (JCPDS card 26-0768: $a = 6.658$ Å, $b = 8.784$ Å, $c = 4.9266$ Å, $\beta = 102.48°$). It is worth mentioning that XRD results for the nanoribbons and hierarchical nanostructures which will be introduced later in this report all showed the same monoclinic $In_2Ge_2O_7$ crystal phase.

Detailed crystal structures of the nanowires were further characterized by TEM. Figure 2a is a typical low magnification

* Corresponding author. Phone: (65)-67906661; fax: (65)-67909081; e-mail: pslee@ntu.edu.sg.
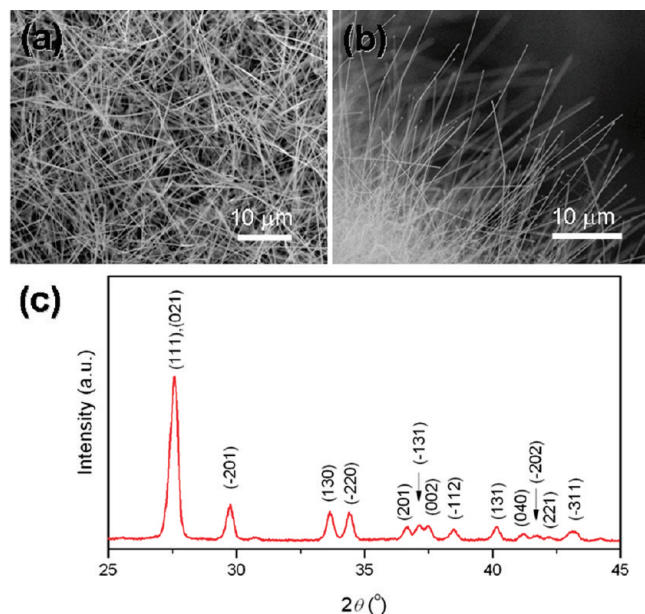
Figure 1. (a, b) FESEM images of the as-synthesized nanowires on substrates; (c) XRD pattern of the $In_2Ge_2O_7$ nanowires.
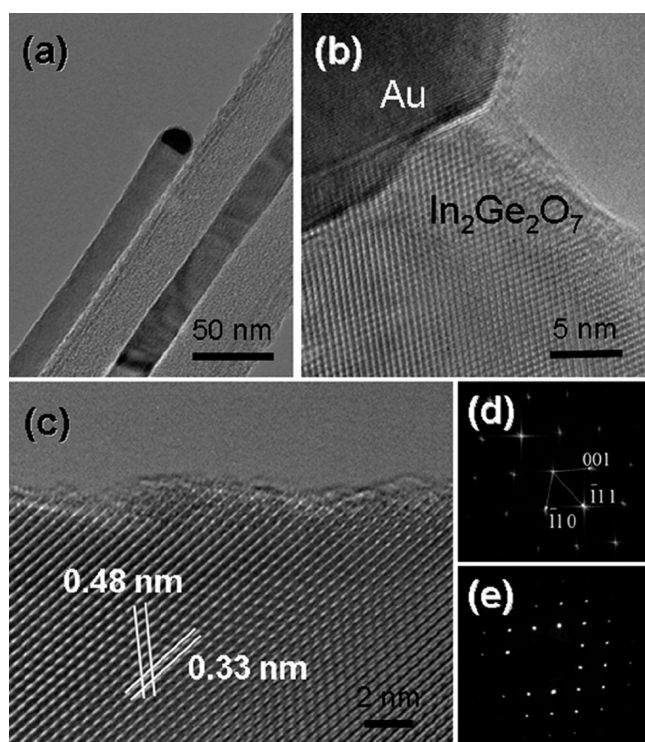

Figure 2. (a) Low magnification TEM image of the $In_2Ge_2O_7$ nanowire with metal catalyst particle at the front; (b) HRTEM image of nanowire segment below catalyst; (c) lattice-resolved HRTEM image of the nanowire; (d) two-dimensional Fourier transform along the [110] zone axis; (e) corresponding SAED pattern of the nanowire.

TEM image of the $In_2Ge_2O_7$ nanowires. Au catalyst particle can be clearly viewed at the growth front (dark region), indicating that the nanowires are synthesized via a VLS mechanism.[12] An HRTEM image of the nanowire segment right below the catalyst particle is shown in Figure 2b. Lattice-resolved HRTEM image of the nanowire is shown in Figure 2c, with its corresponding two-dimensional (2D) fast Fourier transform (FFT) and selected area electron diffraction (SAED)
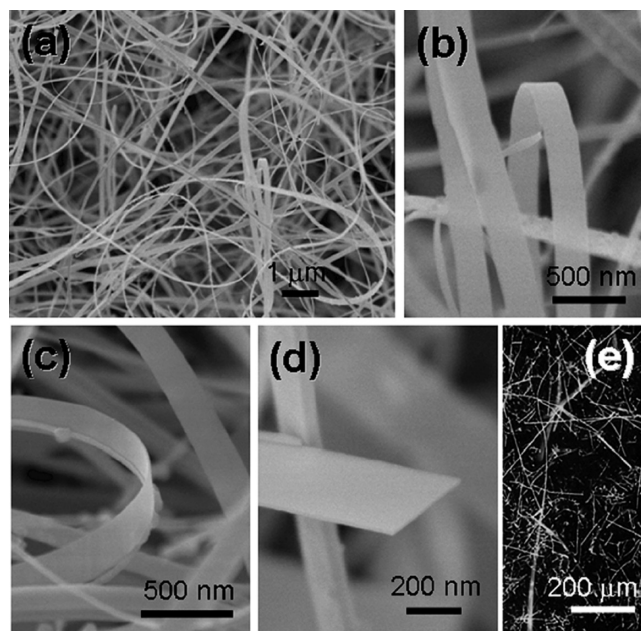

Figure 3. (a) Low magnification FESEM image of the $In_2Ge_2O_7$ nanoribbons; (b, c) magnified FESEM images showing the curved nanoribbon morphology; (d) FESEM image of the nanoribbon cross-section; (e) low magnification optical microscopy image showing the ultralong nanoribbons.

pattern shown in Figure 2d,e, respectively. HRTEM analyses confirm that all the nanowires are single crystalline with no structure defects observed in the nanowire volume. The FFT as well as SAED pattern agrees well with the [110] zone axis of monoclinic $In_2Ge_2O_7$. Measured lattice spacing of 0.48 and 0.33 nm corresponds to the spacing between (001) and ($\bar{1}$11) planes. Growth direction of the nanowire is close to the (001) axis of the $In_2Ge_2O_7$ crystal.

3.2. Indium Germanate Nanoribbon Growth. While pure Ar was used as the carrier gas for $In_2Ge_2O_7$ nanowire synthesis, nanoribbons were successfully synthesized through the introduction of O_2 into the reaction chamber. In a typical nanoribbon synthesis reaction, Ar gas mixed with 5% O_2 at a total flow rate of 200 sccm was used as the carrier gas. White fluffy layers of several millimeters extending from the substrate surface can be clearly observed when the furnace was cooled down. Figure 3a shows the representative morphology of $In_2Ge_2O_7$ nanoribbons synthesized using mixed carrier gas (5% O_2). Magnified FESEM images revealing the unique curved nanoribbon shape are shown in Figure 3b,c. FESEM image of the nanoribbon cross-section is shown in Figure 3d. The width and thickness of the nanoribbon measured from the cross-section are 330 and 15 nm, with a corresponding width-to-thickness ratio of 22. The lengths of the as-synthesized nanoribbons are several hundreds of micrometers or even up to millimeters. Typical low magnification dark-field optical microscopy image showing the ultralong nanoribbons is presented in Figure 3e.

Controlled experiments using mixed carrier gas of different O_2 concentrations showed that the nanoribbon growth temperature increased with O_2 content. For example, nanoribbon growth using carrier gas with 5% and 10% O_2 was observed in the temperature range of 620−700 °C and 750−800 °C, respectively.

Morphology, crystal structure, and composition of the nanoribbons were further characterized using TEM and EDS. Figure 4a is a representative low magnification TEM image of the $In_2Ge_2O_7$ nanoribbon. The ripple-like contrast is due to the strain
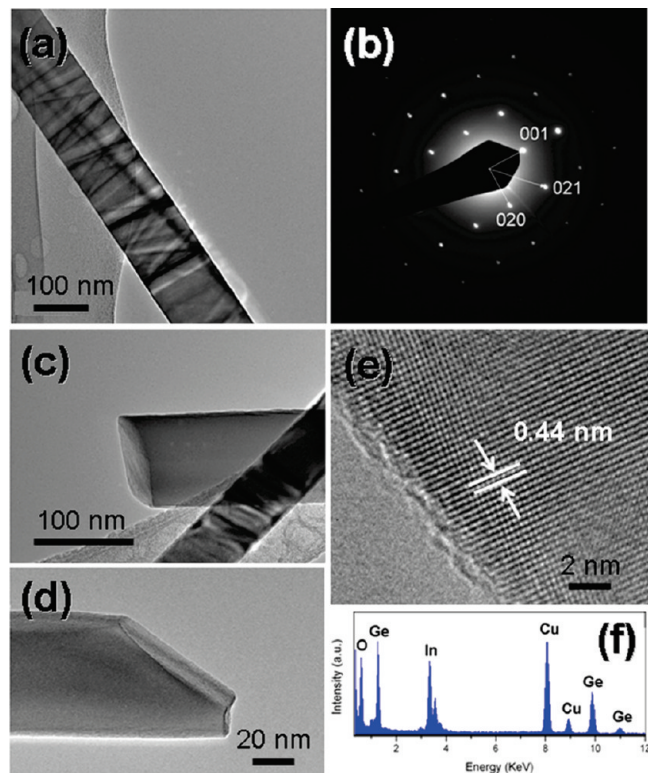
Figure 4. (a) TEM image of a single $In_2Ge_2O_7$ nanoribbon; (b) SAED pattern of the nanoribbon along [100] zone axis; (c, d) TEM images showing the cross sections of the nanoribbons; (e) HRTEM image and (f) EDS spectrum of the nanoribbons.

that resulted from the bending of the nanoribbon.[20] SAED pattern of the nanoribbon taken along the [100] zone axis is shown in Figure 4b. HRTEM image of the nanoribbon is shown in Figure 4e, and the measured lattice spacing of 0.44 nm corresponds to the spacing between (020) planes of monoclinic $In_2Ge_2O_7$. Upon taking the SAED pattern and HRTEM image into account, one can suggest that the preferred growth direction of the nanoribbon is close to the [010] axis of the monoclinic structure. TEM images of the rectangular cross sections of the nanoribbons are shown in Figure 4c,d. In comparison with the symmetric cross sections of nanowires (such as circular, square, or hexagonal), the rectangular cross sections with a large width-thickness ratio represent the distinct ribbon-like morphology. Careful examinations showed that no metal catalyst particles could be observed at the ends the nanoribbons, which is consistent with FESEM observation (see Figure 3d). Thus, the VLS process may not be the dominant growth mechanism for nanoribbon formation. Finally, chemical composition of the nanoribbons was analyzed using EDS. EDS results (Figure 4f) reveal that the nanoribbons are composed of In, Ge, and O, with an atomic ratio of In/Ge around 1:1. Peaks of Cu come from the Cu grid used for TEM characterization.

3.3. Hierarchical Indium Germanate Nanostructure Growth. Three-dimensional (3D) hierarchical $In_2Ge_2O_7$ nanostructures were synthesized using Ge and In as raw material through a similar thermal evaporation process. The deposited material in the as-synthesized sample has a dominant morphology consisting of aligned $In_2Ge_2O_7$ nanowire arrays standing on top of large microcrystals (Figure 5a). Enlarged FESEM images clearly reveal the nanowire arrays growing on polygonous microcrystals (Figure 5b) or microrods (Figure 5c). Magnified view of the joint section of the aligned nanowire array is shown in Figure 5d. The thin nanowires have dimensions of 10−50

nm in diameter and 0.5−2 μm in length. Typically, the diameter of the joint section is slightly larger than that of the nanowire (Figure 5c,d). In the as-synthesized sample, the microcrystals are in close vicinity to each other (Figure 5a,b), and it is possible for the orientation-aligned nanowire arrays to form crossed nanowire networks. Representative parallel and crossed nanowire networks are shown in Figure 5, panels e and f, respectively.

Figure 6a is a typical low magnification TEM image showing the oriented growth of thin $In_2Ge_2O_7$ nanowires on top of the microcrystals. Dashed circle indicates a curved nanowire tip, while most of the nanowires are straight. Enlarged views of the tip and bottom of the nanowire array are shown in Figure 6b,c. Metal catalyst particle can be clearly observed at the nanowire growth fronts (Figure 6b). Figure 6d is a representative TEM image of the bottom of a single nanowire growing on microcrystal, and corresponding HRTEM images with locations indicated by squares in Figure 6d are shown in Figure 6e−g. Measured lattice spacing of 0.52 nm in Figure 6f,g corresponds to the spacing between ($1\bar{1}0$) planes of monoclinic $In_2Ge_2O_7$. Growth direction of the thin nanowires is close to the [001] direction as determined from the FFT pattern (Figure 6e inset). HRTEM image of the nanowire−microcrystal junction (Figure 6g) clearly shows the crystal continuity, suggesting that the microcrystals serve as epitaxial templates for VLS nanowire growth. Similar oriented growth of nanowire arrays on large microcrystals have previously been reported for several other materials.[21−23]

3.4. Growth Mechanisms. According to the VLS mechanism, metal catalyst particles serve as preferential adsorption sites due to the large accommodation coefficient, and precipitation at the liquid−solid interface leads to the anisotropic growth of nanowires.[12] Since metal catalyst particles can be clearly observed at the growth fronts of the as-synthesized $In_2Ge_2O_7$ nanowires (Figure 2a), we suggest that the nanowires are grown via a VLS mechanism. In principle, low melting point vapor species, such as In, In_2O, Ge, or GeO, were generated by carbon thermal reduction processes at high temperature. The chemical vapor species were brought to the low temperature region by Ar flow and would be preferentially adsorbed to the Au droplet surface. Continuous adsorption of those vapor species led to the precipitation of solid $In_2Ge_2O_7$ nanowires when combined with residual oxygen in the furnace.[17]

VS growth involving direct raw materials vaporization and condensation has been most widely employed to explain the formation of nanoribbons in vapor phase.[3] However, unlike the well-developed VLS process, the detailed growth processes of the VS mechanism are still not fully understood.[20,24,25] In general, surface energy and growth kinetics are the two key factors determining the final morphology of the products.[20] There is a strong tendency to minimize the total surface energy during nanostructure nucleation and growth processes. Other factors that affect crystal growth kinetics may also play important roles in the formation of belt-like nanostructures, such as ambient gas, heating history, growth temperature, or even the growth chamber geometry.[3,26−28]

Here we propose a possible process that may account for the ultralong and uniform $In_2Ge_2O_7$ nanoribbon formation in our experiments. At the initial stage, nucleations of nanoclusters form on the substrate surface through direct vapor deposition at the low temperature region. The nanoclusters tend to be enclosed by low energy facets in order to minimize the total surface energy. Both theoretical and experimental studies have revealed a similar surface energy minimization tendency for nanowire nucleation and growth.[29,30] These low energy facets
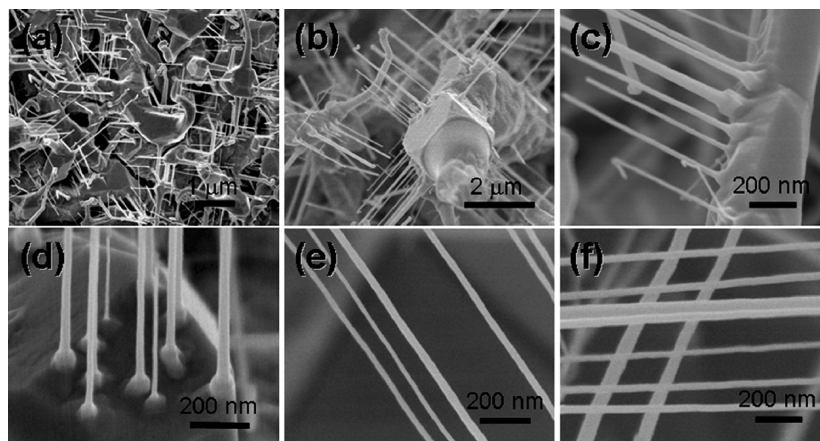
Figure 5. (a) Low magnification FESEM image of the hierarchical $In_2Ge_2O_7$ nanostructures; (b−d) magnified FESEM images showing $In_2Ge_2O_7$ nanowires growing on microcrystals; FESEM image of the (e) parallel and (f) crossed nanowire configurations.
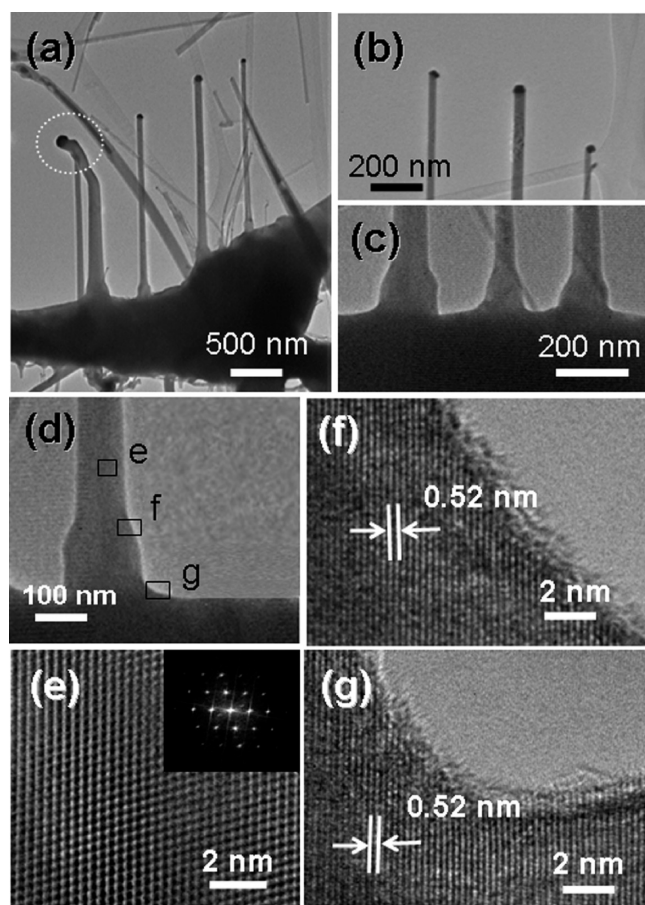

Figure 6. (a) TEM image of the hierarchical $In_2Ge_2O_7$ nanostructures; (b, c) magnified TEM images of the tip and bottom of the nanowire array; (d) representative TEM image of the bottom of a single nanowire growing on microcrystal; (e−g) HRTEM images of the nanowire with locations indicated in (d). Inset in (e) is the corresponding two-dimensional Fourier transform recorded along the [110] zone axis.

should be slow growing facets and require a high supersaturation for nucleation.[26] On the other hand, the top surface of the clusters may not likely be low energy facets due to the crystal symmetry constraints.[26] As a result, newly arriving growth species will not remain on the flat low energy side facets and tend to diffuse toward the atomically rough growth fronts with steps, ledges, and kinks.[20] The nanoribbon length increases

rapidly due to the continuous preferential nucleation and incorporation of growth species at the top surface.

One critical issue to be addressed is what determines the cross section shape of the nanoribbons to be rectangular. Previous research work on whisker growth showed that the 2D nucleation probability on whisker surface can be described as[25,31]

$$P_N = B \exp\left(-\frac{\pi\sigma^2}{k^2 T^2 \ln \alpha}\right) \quad (1)$$

where P_N is the nucleation probability, B is a constant, σ is the surface energy, k is the Boltzmann constant, T is the absolute temperature and α is the supersaturation ratio defined by $\alpha = p/p_0$ (usually $\alpha > 1$), where p is the actual vapor pressure, and p_0 is the equilibrium vapor pressure corresponding to temperature T. As revealed in the equation, lower surface energy corresponds to a higher 2D nucleation probability. In other words, the surface areas of the low energy surfaces tend to increase in order to minimize the total surface energy. Also, a higher temperature and larger supersaturation ratio facilitate the 2D nucleation, resulting in the formation of a sheet-like structure.[25] In contrast, lower temperature and smaller supersaturation ratio promote the elongation along the axial direction and lead to the growth of wire-like structures.[25] In our experiments, introduction of O_2 mainly has two effects. First, growth temperature increases with O_2 concentration. For example, the nanoribbon growth temperature using carrier gas with 5% and 10% O_2 are in the range of 620−700 °C and 750−800 °C, respectively. Second, the vapor supersaturation ratio increases with O_2 concentration due to the faster oxidation rate. The higher growth temperature (T) and higher supersaturation ratio (α) along with the introduction of O_2 would increase the 2D nucleation probability of the low energy side facets, resulting in lateral growth (increase of surface area) of the side facets. Moreover, as viewed from the cross sections of the nanoribbons (Figures 3d and 4c), formation of the slightly anisotropic rectangular shape is due to the different surface energies (σ) and thus different growth rates (according to eq 1) of the two groups of side facets. The effect of side facets growth rate has been reported previously for the WO_3 nanoribbon growth.[32]

We suggest that the 2D growth of the side facets is only significant at the nucleation and initial growth stage. The low energy side facets may not be atomically flat at the nucleation stage and have steps and ledges. The slightly different growth

rates lead to the formation of rectangular cross sections. 2D growth of the side facets is negligible after a short growth period when the side facets are atomically flat. This is consistent with the experimental fact that the diameters of the In$_2$Ge$_2$O$_7$ nanoribbons are very uniform with lengths up to millimeters and no tapering was observed. Previous research work on nanoribbon growth also showed negligible tapering of the nanoribbons although they are ultralong in length.[3,20] Other growth kinetic related factors may also play important roles in the formation of the In$_2$Ge$_2$O$_7$ nanoribbons and further study is needed to clarify the possible effects.

A combination of the VS and VLS mechanism can be used to explain the growth process of the In$_2$Ge$_2$O$_7$ hierarchical nanostructures. First, the Ge and In vapor mixture, generated by evaporation of raw material at the center of the furnace (high temperature region), underwent a fast condensation and reaction process at the low temperature region when combined with residual O$_2$ in the chamber. Large In$_2$Ge$_2$O$_7$ microcrystals formed on the substrate surface via a VS dominant process, possibly with the assistance of Au.[21] Second, parts of the Au nanoparticles were elevated and remained on the surface when the crystals grew large. Consequently, the Au nanoparticles served as catalysts for the growth of thin nanowires. Composition of the Au catalyst particles were confirmed using EDS (not shown). The Au catalysts were crucial in the formation of In$_2$Ge$_2$O$_7$ microcrystals and aligned nanowire arrays, analogous to previous report.[21] We were not able to obtain the hierarchical nanostructures in controlled experiments without Au while other conditions were kept unchanged. The formation of aligned nanowire arrays is due to the homoepitaxial growth considering the same composition of the microcrystal and nanowire. The crystallographic epitaxial relationship of the nanowires and other initially formed structures has been demonstrated previously in the homoepitaxial growth of several other materials.[21,22,33]

It is also well-known that the structures and morphologies of the products can be greatly influenced by the source materials. In this report, we have shown that In$_2$Ge$_2$O$_7$ nanowires were produced by using GeO$_2$ and In$_2$O$_3$ as source materials, while hierarchical structures were produced when Ge and In was used as source materials with other growth conditions kept unchanged. Many other reports have also confirmed the great influence of the source materials. For example, In$_2$O$_3$ nanoarrows were produced by using In as source material, while In$_2$O$_3$ nanorods were produced by using In$_2$O$_3$ and carbon as source materials.[34] Also, ZnO nanobelts were produced by using ZnO as the source material;[3] however, ZnO nanorings were produced by adding In$_2$O$_3$ and lithium carbonate into the source material.[35] The source materials may affect the evaporation and condensation kinetics during the vapor deposition processes, but the details still need to be clarified.

4. Conclusions

In conclusion, morphology controlled 1D In$_2$Ge$_2$O$_7$ nanostructures (nanowires, nanoribbons, and hierarchical nanostructures) were synthesized by a thermal evaporation method. The successful morphology control was achieved by properly selecting the experimental conditions, such as catalyst, carrier gases, and source materials. The nanowires, ultralong nanoribbons, and hierarchical nanostructures were synthesized via VLS, VS, and a combination of VLS and VS processes, respectively. Surface energy and growth kinetics play important roles in

determining the morphology of the nanoribbons with rectangular cross sections. Furthermore, it is suggested that In$_2$Ge$_2$O$_7$ microcrystals serve as epitaxial templates for thin nanowire growth, resulting in the formation of aligned nanowire arrays. The methods to control the nanostructure morphologies and thus their properties may provide insights for nanostructure synthesis and facilitate their potential applications.

References

(1) Charlier, J. C.; DeVita, A.; Blase, X.; Car, R. *Science* **1997**, *275*, 646.
(2) Morales, A. M.; Lieber, C. M. *Science* **1998**, *279*, 208.
(3) Pan, Z. W.; Dai, Z. R.; Wang, Z. L. *Science* **2001**, *291*, 1947.
(4) Zimmler, M. A.; Stichtenoth, D.; Ronning, C.; Yi, W.; Narayanamurti, V.; Voss, T.; Capasso, F. *Nano Lett.* **2008**, *8*, 1695.
(5) Huang, Y.; Duan, X. F.; Lieber, C. M. *Small* **2005**, *1*, 142.
(6) Hochbaum, A. I.; Chen, R. K.; Delgado, R. D.; Liang, W. J.; Garnett, E. C.; Najarian, M.; Majumdar, A.; Yang, P. D. *Nature* **2008**, *451*, 163.
(7) Cui, Y.; Wei, Q. Q.; Park, H. K.; Lieber, C. M. *Science* **2001**, *293*, 1289.
(8) Mazeina, L.; Picard, Y. N.; Prokes, S. M. *Cryst. Growth Des.* **2009**, *9*, 1164.
(9) Liu, Z.; Zhang, X. T.; Hark, S. K. *Cryst. Growth Des.* **2009**, *9*, 803.
(10) Milliron, D. J.; Hughes, S. M.; Cui, Y.; Manna, L.; Li, J. B.; Wang, L. W.; Alivisatos, A. P. *Nature* **2004**, *430*, 190.
(11) Cao, F.; Shi, W. D.; Zhao, L. J.; Song, S. Y.; Yang, J. H.; Lei, Y. Q.; Zhang, H. J. *J. Phys. Chem. C* **2008**, *112*, 17095.
(12) Wanger, R. S.; Ellis, W. C. *Appl. Phys. Lett.* **1964**, *4*, 89.
(13) Gier, T. E.; Bu, X. H.; Feng, P. Y.; Stucky, G. D. *Nature* **1998**, *395*, 154.
(14) Hogan, M. J.; Brinkman, A. W.; Hashemi, T. *Appl. Phys. Lett.* **1998**, *72*, 3077.
(15) Liu, G. Z.; Zheng, S. T.; Yang, G. Y. *Angew. Chem., Int. Ed.* **2007**, *46*, 2827.
(16) Bayya, S. S.; Chin, G. D.; Sanghera, J. S.; Aggarwal, I. D. *Opt. Express* **2006**, *14*, 11687.
(17) Zhan, J. H.; Bando, Y.; Hu, J. Q.; Yin, L. W.; Yuan, X. L.; Sekigitchi, T.; Golberg, D. *Angew. Chem., Int. Ed.* **2006**, *45*, 228.
(18) Su, Y.; Li, S.; Xu, L.; Chen, Y. Q.; Zhou, Q. T.; Peng, B.; Yin, S.; Meng, X.; Liang, X. M.; Feng, Y. *Nanotechnology* **2006**, *17*, 6007.
(19) Yan, C. Y.; Zhang, T.; Lee, P. S. *Cryst. Growth Des.* **2008**, *8*, 3144.
(20) Wang, Z. L. *Adv. Mater.* **2003**, *15*, 432.
(21) Chen, X.; Kim, M. H.; Zhang, X.; Larson, C.; Yu, D.; Wodtke, A. M.; Moskovits, M. *J. Phys. Chem. C* **2008**, *112*, 13797.
(22) Gao, P. X.; Ding, Y.; Wang, Z. L. *Nano Lett.* **2003**, *3*, 1315.
(23) Moore, D. F.; Ding, Y.; Wang, Z. L. *J. Am. Chem. Soc.* **2004**, *126*, 14372.
(24) Moore, D.; Wang, Z. L. *J. Mater. Chem.* **2006**, *16*, 3898.
(25) Dai, Z. R.; Pan, Z. W.; Wang, Z. L. *Adv. Funct. Mater.* **2003**, *13*, 9.
(26) Wacaser, B. A.; Dick, K. A.; Johansson, J.; Borgstrom, M. T.; Deppert, K.; Samuelson, L. *Adv. Mater.* **2009**, *21*, 153.
(27) Gao, T.; Wang, T. H. *J. Phys. Chem. B* **2004**, *108*, 20045.
(28) Kirkham, M.; Wang, Z. L.; Snyder, R. L. *Nanotechnology* **2008**, *19*, 445708.
(29) Wang, C. X.; Hirano, M.; Hosono, H. *Nano Lett.* **2006**, *6*, 1552.
(30) Schmidt, V.; Senz, S.; Gosele, U. *Nano Lett.* **2005**, *5*, 931.
(31) Blakely, J. M.; Jackson, K. A. *J. Chem. Phys.* **1962**, *37*, 428.
(32) Li, Y. B.; Bando, Y.; Golberg, D.; Kurashima, K. *Chem. Phys. Lett.* **2003**, *367*, 214.
(33) Seo, K.; Varadwaj, K. S. K.; Cha, D.; In, J.; Kim, J.; Park, J.; Kim, B. *J. Phys. Chem. C* **2007**, *111*, 9072.
(34) Yan, Y. G.; Zhang, Y.; Zeng, H. B.; Zhang, J. X.; Cao, X. L.; Zhang, L. D. *Nanotechnology* **2007**, *18*, 175601.
(35) Kong, X. Y.; Ding, Y.; Yang, R.; Wang, Z. L. *Science* **2004**, *303*, 1348.